Layer coupling between solutal and thermal convection in liquid metal batteries

Personnettaz, P.; Klopper, T. S.; Weber, N.; Weier, T.;

Highlights

Layer coupling between solutal and thermal convection in liquid metal batteries

Paolo Personnettaz, Tanja Sophia Klopper, Norbert Weber, Tom Weier

- thermal convection appears first in the electrolyte – at charge and discharge

- solutal convection emerges much faster and stronger than thermal convection

- solutal convection can mix bottom layers by viscous coupling, thermal convection not

- solutal convection affects internally heated convection in the electrolyte

- a coupled top interface allows for better mixing in the positive electrode than no-slip

Layer coupling between solutal and thermal convection in liquid metal batteries

Paolo Personnettaz[a,1,*], Tanja Sophia Klopper[a,b,1], Norbert Weber[a], Tom Weier[a]

[a]*Helmholtz-Zentrum Dresden – Rossendorf, Bautzner Landstr. 400, 01328 Dresden, Germany*
[b]*Carl von Ossietzky University Oldenburg, Ammerländer Heerstr. 114-118, 26129 Oldenburg, Germany*

Abstract

For longer than one decade, liquid metal batteries (LMBs) are developed with the primary aim to provide economic stationary energy storage. Featuring two liquid metal electrodes separated by a molten salt electrolyte, LMBs operate at elevated temperature as simple concentration cells. Therefore, efficient mass transfer is a basic prerequisite for their economic operation. A thorough understanding of the relevant mechanisms cannot be achieved by studying single layers in isolation. With this motivation, the effects of solutal- and thermally-driven flow are studied, as well as the flow coupling between the three liquid layers of the cell. It is shown that solutal convection appears first and thermal convection much later. While the presence of solutal flow depends on the mode of operation (charge or discharge), the occurrence of thermal convection is dictated by the geometry (thickness of layers). The coupling of the flow phenomena between the layers is intriguing: while thermal convection is confined to its area of origin, i.e. the electrolyte, solutal convection is able to drive flow in the positive electrode and in the electrolyte.

Keywords: liquid metal battery, mixing, solutal convection, Rayleigh-Bénard convection, internally heated convection, layer coupling

---

*Corresponding author. Helmholtz-Zentrum Dresden – Rossendorf, Bautzner Landstr. 400, 01328 Dresden, Germany. *E-mail address*: p.personnettaz@hzdr.de (P. Personnettaz)
[1]The two first authors contributed equally to the publication.

1. Introduction

Since the turn of the millennium, liquid metal batteries (LMBs) are discussed as low-cost stationary electrical energy storage for fluctuating renewable sources. Figure 1 illustrates the typical setup of such a device. The negative electrode on top is separated from the positive electrode by a thin molten salt electrolyte layer [1]. In order to prevent a short-circuit between the electrodes, violent fluid flow needs to be avoided [2].
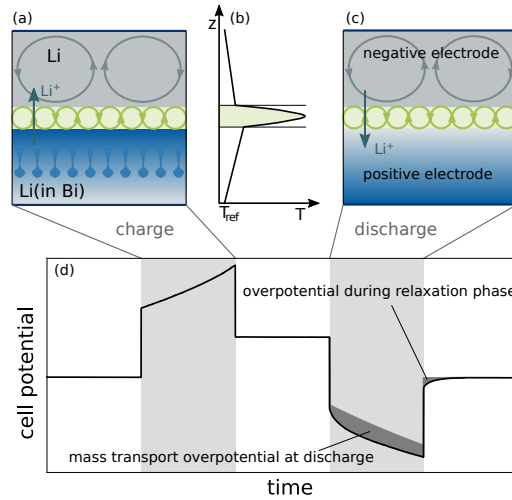

Figure 1: Setup and operation of a Li||Bi LMB at charge (a) and discharge (c) as well as the pure conduction vertical temperature profile during operation (b). Sub-figure (d) illustrates a charge-discharge cycle with typical effects due to mass transport overvoltage [3].

LMBs are simple concentration cells. At discharge, the electro-active species migrates from the negative electrode through the electrolyte before being alloyed into the positive electrode. It has already been noticed during the first days of LMB research that non-ideal mixing during this alloying process leads to mass transport overpotentials. A highly concentrated solute region located near the interfaces will develop especially at high current density [4]. In extreme cases, even solid intermetallic phases might form at the electrolyte-positive electrode interface [5, 6]. Convection [6] and mechanical stirring [5, 7] have been proposed to mitigate concentration overpotentials.

In recent years, many flow effects have been investigated aiming to enhance mass transfer in liquid metal electrodes. Electro-vortex flow (EVF),

2

which is driven by converging or diverging current lines, has been explored by Ashour et al. [8]. Shortly after, it has been shown that the placement of the feeding lines as well as stray magnetic fields have a critical influence on the flow structure and magnitude of EVF [9]. Using an energy balance and numerical modelling, Herreman et al. concluded that non-swirling electro-vortex flow is too weak to break the stable density stratification during discharge inside the positive electrode [10].

Recently, Weber et al. [11] combined convection with an electrochemical model showing that the influence of EVF on the cell voltage is indeed limited. On the other hand, a vertical magnetic background field, which drives strong swirling flow, is able to increase the cell efficiency substantially. The latter has been confirmed theoretically and with direct numerical simulations by Herreman et al. as well [12].

Thermal convection in LMBs has been subject of various investigations. Motivated by mixing the positive electrode alloy, Kelley & Sadoway heated a Pb-Bi layer from below measuring the flow velocity [13]; the experiment was later reproduced numerically by Beltrán [14]. Shen & Zikanov [15] were the first who modelled thermal convection in a complete LMB. They show that it is caused mainly by the heat released in the electrolyte, as illustrated in Figure 1b. Consequently, flow is expected to appear in the negative electrode and electrolyte, while the positive electrode is stably stratified. Flow structures and magnitude depend very much on the thickness of the single layers. Köllner et al. [16] confirmed these early investigations and pointed out the presence of three additional thermally driven flows: Marangoni flows at both interfaces and anti-convection in the lower layer. Finally, Personnettaz et al. [17] discussed the presence of electrochemical heat, and highlighted that in realistic LMBs with thin electrolyte layers (5 mm) thermal convection will be dominant in the thick negative electrode, but negligible in the electrolyte itself.

While thermal convection and EVF appear independently of the direction of the current, solutal convection can be observed only at charge. As illustrated in Figure 1a for a Li||Bi cell, Li is transferred from the positive electrode alloy towards the negative electrode. The heavy (Li-poor) Bi-Li alloy will sink down in plumes. At discharge, this process is reversed: Li is alloyed on top of the Bi-rich layer forming a stable density stratification (Figure 1c). This "asymmetry" of the effects leads to an "asymmetry" within the corresponding charge-discharge curve, shown in Figure 1d. At discharge a considerable mass transport overpotential is observed, which is not present

3

while charging. When switching off the current, the voltage returns immediately to the equilibrium potential after a charging phase (solutal flow), but needs a certain diffusive relaxation time after a discharge phase (stable density stratification). The crucial relevance of solutal convection and the stable density stratification has to our knowledge first been discussed by Kelley & Weier [2] and has for the first time been evidenced by Personnettaz et al. [3]. The findings have later been confirmed by Herreman et al. [10]; they performed two- and three-dimensional numerical simulations of mass transport and EVF. Interestingly, the two mass transfer polarization effects, highlighted in Figure 1d can also be observed in older measurements. For example, the charge-discharge curve of a Na||Bi cell from 2015 shows an additional overpotential at discharge [18], and Fig. 8b in Kim et al. [19] displays a relaxation of the cell potential after a discharge cycle. Tab. 1 gives a few more examples of related effects in the literature. The aim of this

Table 1: Experimental results showing mass transport overvoltage in the literature of liquid metal electrodes. Chronological order.

observation	source
polarization effects at high discharge current in Li-Cd and Li-Zn cells	[20, p. 202]
clear concentration polarization, when switching off current after discharge	[21, p. 75]
strong asymmetry of interface concentration between charge and discharge	[22, p. 955]
clear concentration polarization effects after switching off the current	[23, p. 159]
charge-discharge curve shows additional (concentration) losses at discharge	[18]

article is to elucidate the interaction between solutal and thermal convection in particular during the transient start-up of the battery. In this context, we pay special attention to the coupling of the flow between the three distinct layers. In the first part of the article, we state the relevant equations that describe thermal and solutal convection in three-layer LMBs. From them, we deduce the relevant dimensionless number and we provide estimations of the expected orders of magnitude for different chemistries. Previous studies are then used to compute the critical current density at which thermal convection appears in the two top layers. Then, we move to the numerical modelling of 2D Li||Bi cells during charge and discharge. There, we discuss the effect of sign and magnitude of the current on heat, mass and momentum transfer.

2. Theory

The distinct regions $\Omega^{(i)}$ (N-negative electrode, E-electrolyte, P-positive electrode) of an LMB are coupled at their interfaces $\partial\Omega^{(i|j)}$, see Figure 3. They permit the exchange of momentum, heat and – for certain ions – mass through electrochemical reactions. The transport processes inside the regions depend on the boundary conditions and material properties. These vary widely from layer to layer and so do the transport phenomena. In this section we will discuss the equations describing these mechanisms, we will rearrange the relevant parameters in the form of dimensionless numbers and provide indications on the presence of convection in the different layers.

2.1. Mass transport

Mass transport is vital for the operation of electrochemical cells. In the negative electrode of LMBs, concentration gradients are typically absent because it consists in many cases of a pure substance (but see Ca-Bi||Ca-Sb [24], Ca-Mg||Bi [25] and Li-Mg||Sb-Pb [26] for counterexamples). In this work, we neglect the presence of advective and diffusive transport of ions in the electrolyte. Postulating a perfectly blended electrolyte seems justified by experimental evidence [27]. Therefore, concentration distributions are considered only in the positive electrode, assuming a binary mixture A-B (in the present study Li-Bi). The mass concentration of component A, ρ_A ($\mathrm{kg\,m^{-3}}$), is described by the advection-diffusion equation [3, 10, 28]

$$\frac{\partial \rho_A}{\partial t} + \mathbf{u} \cdot \nabla \rho_A = \mathcal{D}_{AB} \nabla^2 \rho_A \text{ in } \Omega^{(P)}, \tag{1}$$

in which $\mathbf{u}$ is the velocity field and $\mathcal{D}_{AB}$ is the mass transport diffusion coefficient. We neglect the volume change of the positive electrode due to the density variation as well as the concentration dependency of the diffusion coefficient [29]. As the solid boundaries are impermeable, we impose an homogeneous Neumann condition for the concentration. The interface between the electrolyte and the positive electrode allows for the transfer of mass, because ions are reduced or oxidised there as $A^+ + e^- \leftrightharpoons A(\text{in}B)$ through electrochemical reactions. The mass flux of the component A under amperostatic conditions, $\dot{m}_A''$, can be computed with the Faraday law of electrolysis. The resulting boundary condition can be formulated then as

$$-\mathcal{D}_{AB} \nabla \rho_A \cdot \mathbf{n} = \dot{m}_A'' = \frac{j \mathcal{M}_A}{n_{el} F} \text{ at } \partial\Omega^{(P|E)}, \tag{2}$$

5

where j, $\mathcal{M}_A$, $\mathbf{n}$, n_{el}, F are current density, molar mass of the component A (Li in our application), the surface normal vector, the number of charges exchanged by the electrochemical reaction and the Faraday constant, respectively. We consider only the primary current distribution, which is uniform in the whole domain, assuming that the top and bottom plate are ideal current collectors and that the lateral walls are insulated.

2.2. Heat transport

In LMBs, heat is mainly generated by the passage of an electrical current through the electrolyte, and then transported into the full cell. For an overview of thermal phenomena in LMBs and the relevant assumptions, please refer to Personnettaz et al. [17]. The transport equation for the temperature T in the i-th layer reads

$$\frac{\partial T}{\partial t} + \mathbf{u} \cdot \nabla T = \mathcal{D}_T^{(i)} \nabla^2 T + \frac{\mathcal{D}_T^{(i)}}{k^{(i)}} (\dot{q}''')^{(i)} \text{ in } \Omega^{(i)} \text{ for } i = \mathrm{N, E, P}, \qquad (3)$$

in which $\mathcal{D}_T$ and k are thermal diffusivity and conductivity. The ohmic internal heat generation is described by $\dot{q}''' = \rho_{el} j^2$, in which ρ_{el} is the electrical resistivity. Electrochemical heat generation is completely neglected. The top and bottom boundaries are kept at uniform temperature T_{ref}. Lateral sides are assumed adiabatic. At the interfaces between the layers, $\partial \Omega^{(i|j)}$, continuity of temperature and heat flux must be enforced. Most of these assumptions are shared by previous works [15–17].

2.3. Fluid flow

Adjacent phases in LMBs are immiscible. We work in the assumption of fixed interfaces and of the Boussinesq approximation, similar as previous authors [15, 16]. The momentum balance is defined as

$$\frac{\partial \mathbf{u}}{\partial t} + \mathbf{u} \cdot \nabla \mathbf{u} = -\frac{1}{\rho_{ref}^{(i)}} \nabla p_d + \nu^{(i)} \nabla^2 \mathbf{u}$$
$$- (\beta_T^{(i)} (T - T_{ref}) + \beta_{\rho_A}^{(k)} (\rho_A - \rho_{A,ref})) \mathbf{g} \text{ in } \Omega^{(i)} \text{ for } i = \mathrm{N, E, P} \text{ and } k = \mathrm{P},$$
$$(4)$$

where ρ_{ref} is the density under reference conditions, ν is the kinematic viscosity, p_d is the modified pressure, $\mathbf{g}$ is the gravity acceleration vector and β_T and β_{ρ_A} are thermal and solutal expansion coefficient [30]. We neglect the presence of other body forces, like the one generated by magneto-hydrodynamic

effects. The velocity field satisfies the continuity equation in the incompressible form $\nabla \cdot \mathbf{u} = 0$. At the interfaces, $\partial\Omega^{(i|j)}$, the normal velocity is enforced to be zero. The tangential components are assumed continuous across the interfaces. Furthermore, the stress balance

$$(\rho_{\mathrm{ref}}\nu)^{(\mathrm{i})}\frac{\partial u_k}{\partial z} = (\rho_{\mathrm{ref}}\nu)^{(\mathrm{E})}\frac{\partial u_k}{\partial z} \text{ at } \partial\Omega^{(i|\mathrm{E})} \text{ for } i = \mathrm{N}, \mathrm{P} \text{ and } k = x, y \quad (5)$$

must be satisfied. In this context, the terms accounting for solutal and thermal Marangoni effects are neglected, namely $\nabla_{\mathrm{S}}\gamma^{(i|\mathrm{E})}(T, \rho_{\mathrm{A}})$, in which ∇_{S} is the surface gradient and $\gamma^{(i|\mathrm{E})}(T, \rho_{\mathrm{A}})$ is the interfacial tension [30]. The walls are rigid and impermeable and described by a no-slip boundary condition.

2.4. Dimensionless numbers

The system of equations that describes convective heat and mass transport in a 3-layer LMB contains 18 different material properties, the reference state $(T_{\mathrm{ref}}, \rho_{\mathrm{A,ref}})$, and one operating parameter: the current density j. Furthermore, we have to consider the geometrical dimensions: three layer heights $\Delta h^{(\mathrm{i})}$ and the lateral extension of the cell L_x. This large number of parameters motivates performing a dimensionless analysis. Here, we consider every layer per se and we use as example the positive electrode in which both heat and mass transfer take place. At least five distinct time scales can be defined: three based on diffusion $(\mathcal{T}_{\mathcal{D}i} = \mathcal{L}^2\mathcal{D}_i^{-1})$ and two based on the free fall velocity (e.g. $\mathcal{T}_{\beta\Theta} = \mathcal{L}(g\beta_{\mathrm{T}}\Delta\Theta\mathcal{L})^{-0.5}$), in which $\mathcal{D}_i$, $\mathcal{L}$ and $\Delta\Theta$ are the diffusivity of the i-th component, the reference height and the reference temperature difference, respectively. If we substitute them in the system of equations, the

7

following five dimensionless numbers appear [28]:

$$\text{Prandtl number:} \quad Pr = \frac{\nu}{\mathcal{D}_\text{T}} \quad = \frac{\mathcal{T}_{\mathcal{D}\Theta}}{\mathcal{T}_{\mathcal{D}u}}, \qquad (6)$$

$$\text{Schmidt number:} \quad Sc = \frac{\nu}{\mathcal{D}_\text{AB}} \quad = \frac{\mathcal{T}_{\mathcal{D}\mathcal{C}}}{\mathcal{T}_{\mathcal{D}u}}, \qquad (7)$$

$$\text{Lewis number:} \quad Le = \frac{\mathcal{D}_\text{T}}{\mathcal{D}_\text{AB}} \quad = \frac{\mathcal{T}_{\mathcal{D}\mathcal{C}}}{\mathcal{T}_{\mathcal{D}\Theta}}, \qquad (8)$$

$$\text{Thermal Rayleigh number:} \quad Ra_\Theta = \frac{g\beta_\text{T}\Delta\Theta\mathcal{L}^3}{\mathcal{D}_\text{T}\nu} \quad = \frac{\mathcal{T}_{\mathcal{D}u}\mathcal{T}_{\mathcal{D}\Theta}}{\mathcal{T}_{\beta\Theta}^2}, \qquad (9)$$

$$\text{Solutal Rayleigh number:} \quad Ra_\mathcal{C} = \frac{g\beta_{\rho_\text{A}}\Delta\mathcal{C}\mathcal{L}^3}{\mathcal{D}_\text{AB}\nu} \quad = \frac{\mathcal{T}_{\mathcal{D}u}\mathcal{T}_{\mathcal{D}\mathcal{C}}}{\mathcal{T}_{\beta\mathcal{C}}^2}, \qquad (10)$$

$$\text{Density ratio:} \quad R_\rho = \frac{\beta_{\rho_\text{A}}\Delta\mathcal{C}}{\beta_\text{T}\Delta\Theta} \quad = \frac{\mathcal{T}_{\beta\Theta}^2}{\mathcal{T}_{\beta\mathcal{C}}^2}. \qquad (11)$$

Here, $\Delta\mathcal{C}$ denotes the reference concentration difference across the layer. The first three dimensionless numbers are ratios of diffusivities and related time scales. The two Rayleigh numbers quantify the strength of the buoyancy with respect to dissipative effects of viscosity and component diffusion. Lewis number and density ratio are not essential parameters of the problem, but they are helpful to understand the relative importance of heat and mass transport.

The concentration difference across the positive electrode can be estimated a priori using the boundary conditions of Eq. 2:

$$\Delta\mathcal{C}_\text{apriori} = \frac{\dot{m}_\text{A}''\Delta h^{(\text{P})}}{\mathcal{D}_\text{AB}} = \frac{j\mathcal{M}_\text{A}\Delta h^{(\text{P})}}{n_\text{el}\text{F}\mathcal{D}_\text{AB}} \ . \qquad (12)$$

This value largely overestimates the real difference, as the concentration gradient is present only in a thin region near the interface. Applying a 1D diffusion model a posteriori using the semi-infinite approximation,

$$\Delta\mathcal{C}_\mathcal{D}(t) = \frac{j\mathcal{M}_\text{A}}{n_\text{el}\text{F}\mathcal{D}_\text{AB}}\sqrt{\frac{4\mathcal{D}_\text{AB}t}{\pi}} \ , \qquad (13)$$

allows for a much realistic approximation. This formulation is time dependent; for the analytical solution of the diffusion problem, please refer to [3] and [10]. If solutal convection takes place, the concentration variation across

8

the layer is even lower and we can compute the latter a posteriori by numerical simulations.

The temperature differences within each layer can be estimated applying 1D pure conduction models like the ones presented by Köllner et al. [16] and Personnettaz et al. [17]. Here we use a simplified model based on the assumption that the thermal resistances $(\frac{\Delta h^{(i)}}{k^{(i)}})$ of the two liquid metal electrodes are comparable. Under this condition, the maximum of the temperature is situated at the mid height of the electrolyte, where we expect no vertical heat flux. Therefore, we can split the domain in two in order to decouple the electrodes. The temperature difference across the full height of the i-th electrode can be expressed as

$$\Delta\Theta^{(i)} = \frac{\rho_{\mathrm{el}}^{(\mathrm{E})} j^2 \Delta h^{(\mathrm{E})}}{2} \frac{\Delta h^{(i)}}{k^{(i)}} \text{ for } i = \mathrm{N}, \mathrm{P}. \tag{14}$$

If additional heat fluxes are present at the interfaces, e.g. due to electrochemical reactions, it is sufficient to add them to the first term. In the electrolyte, the maximum temperature variation spans across half of the electrolyte and can be estimated as

$$\Delta\Theta^{(\mathrm{E})} = \frac{\rho_{\mathrm{el}}^{(\mathrm{E})} j^2 (\Delta h^{(\mathrm{E})})^2}{8 k^{(\mathrm{E})}}. \tag{15}$$

This quantity was used as the temperature unit by Köllner et al. [16]. From these three simple formulas, we deduce that the temperature difference will increase quadratically with the current density, but the concentration difference only linearly. We can use Eq. 14 and Eq. 13 to estimate thermal and solutal Rayleigh numbers in the liquid metal electrodes at the same current density. Tab. 2 gives an overview on the estimated dimensionless numbers for different binary mixtures of the positive electrode. In calculating these numbers, we assumed a layer height Δh of $1\,\mathrm{cm}$ for the electrodes and the electrolyte, a current density of $1\,\mathrm{A\,cm^{-2}}$ and electrical resistivity of the salt of $5 \cdot 10^{-3}\,\Omega\,\mathrm{m^{-1}}$. Most of the liquid metal alloys have Prandtl numbers substantially lower than 1. The diffusion of heat in the electrodes is very efficient. It becomes clear that the solutal Rayleigh number is at least two orders of magnitude larger than the thermal Rayleigh number. This suggests that solutal convection will be able to mix the thermally stably stratified positive electrode layer easily during charge. On the other hand, flow induced in the positive electrode by viscous coupling with the electrolyte is expected to be strongly dampened by the compositionally stably stratified layer during

9

discharge. Two exceptions are electrodes made of selenium or tellurium. As both have a considerably lower thermal diffusivity compared to other liquid metals, we expect in such electrodes an interesting competition between heat and mass transfer.

The temperature and concentration unit can also be used to have a first estimation of thermal $Ma_\Theta = \alpha_{\gamma,T}\Delta\Theta\mathcal{L}(\rho_{\text{ref}}\nu\mathcal{D}_T)^{-1}$ and solutal Marangoni numbers $Ma_\mathcal{C} = \alpha_{\gamma,\rho_A}\Delta\mathcal{C}\mathcal{L}(\rho_{\text{ref}}\nu\mathcal{D}_{\text{AB}})^{-1}$, respectively. $\alpha_{\gamma,T}$ and α_{γ,ρ_A} are the temperature and compositional coefficients of the interface tension [30]. These numbers compare the forces due to the surface tension gradients with the dissipative effect of diffusion and viscosity. Köllner et al. [16] defined thermal Marangoni numbers for both interfaces, which are in the order of $1\cdot10^1 - 1\cdot10^2$. An additional solutal Marangoni numbers can be written for the positive electrode-electrolyte interface, using $\alpha_{\gamma,\rho_A} \sim 1\cdot10^{-2}\,\text{m}^3\,\text{s}^{-2}$ from the data of [31]. For a concentration difference of $1\,\text{kg}\,\text{m}^{-3}$ and a unit length of $1\,\text{cm}$, the solutal Marangoni number is in the order of $1\cdot10^6$.

2.5. Onset of convection in the electrolyte and negative electrode

The onset of thermal convection in the negative electrode and electrolyte depends on current density, material properties and layer thicknesses; it can roughly be estimated using critical Rayleigh numbers from stability analysis available in the literature. The Rayleigh number in the negative electrode can be estimated in first approximation combining Eq. (9) and Eq. (14):

$$Ra^{(\text{N})} \approx \frac{g\beta_{\text{T}}^{(\text{N})}\rho_{\text{el}}^{(\text{E})}j^2(\Delta h^{(\text{N})})^4\Delta h^{(\text{E})}}{2k^{(\text{N})}\mathcal{D}_{\text{T}}^{(\text{N})}\nu^{(\text{N})}}. \tag{16}$$

In the negative electrode, the temperature profile is linear for pure conduction, see Figure 1. The top surface is rigid (wall) and at constant temperature, the boundary condition at the bottom surface can be well approximated by a uniform flux from the electrolyte. This configuration with rigid bottom was studied by Sparrow et al. [35]. They found a critical Rayleigh number of $Ra_{\text{cr},\infty} = 1296$ for an infinite laterally extended layer. Köllner et al. [16] performed a linear stability analysis of the three-layer system, and found for the negative electrode a critical Ra of 1290, when the electrolyte is one tenth of the height of the electrodes.

The electrolyte has a parabolic temperature profile due to the Joule heating, as shown in Figure 1. There, the Rayleigh number is well approximated

Table 2: Heat and mass transport dimensionless numbers for different combinations of active materials in the positive electrode. For the sources of the material properties, refer to [32, 33]. The properties of the alloys (A-B) are computed at molar concentration of 10 % of component A. Due to the scarcity of mixture properties we use blending rules, as described in §4. The mass transport diffusivity is estimated with the model proposed by Roy and Chhabra [34]. $Ra_{T,1}$, $Ra_{\rho_A,1}$ are computed considering a $\Delta\Theta = 1\,\mathrm{K}$, $\Delta\mathcal{C} = 1\,\mathrm{kg\,m^{-3}}$, respectively. All values of Ra are given as absolute values. During discharge, Ra_{ρ_A} is negative, Eq. (13) is evaluated at $t = 10\,\mathrm{s}$. Due to the stable temperature distribution, Ra_T is negative as well.

name	T (°C)	Pr	Sc	Le	$Ra_{T,1}$	Ra_T	$Ra_{\rho_A,1}$	Ra_{ρ_A}	R_ρ
Ca-Bi	550	$1.3 \cdot 10^{-2}$	$1.6 \cdot 10^1$	$1.2 \cdot 10^3$	$7 \cdot 10^2$	$1 \cdot 10^3$	$4 \cdot 10^6$	$3 \cdot 10^8$	9
Ca-Sb	700	$1.7 \cdot 10^{-2}$	$4.0 \cdot 10^1$	$2.3 \cdot 10^3$	$4 \cdot 10^2$	$5 \cdot 10^2$	$4 \cdot 10^6$	$4 \cdot 10^8$	20
K-Hg	250	$3.6 \cdot 10^{-3}$	8.6	$2.4 \cdot 10^3$	$1 \cdot 10^4$	$2 \cdot 10^4$	$1 \cdot 10^8$	$4 \cdot 10^{10}$	20
K-Tl	250	$1.8 \cdot 10^{-2}$	$1.6 \cdot 10^2$	$9.2 \cdot 10^3$	$3 \cdot 10^2$	$3 \cdot 10^2$	$2 \cdot 10^7$	$8 \cdot 10^9$	40
Li-Bi	450	$1.3 \cdot 10^{-2}$	$1.9 \cdot 10^1$	$1.5 \cdot 10^3$	$1 \cdot 10^3$	$2 \cdot 10^3$	$2 \cdot 10^7$	$6 \cdot 10^8$	1
Li-Cd	493	$9.2 \cdot 10^{-3}$	$6.8 \cdot 10^1$	$7.4 \cdot 10^3$	$3 \cdot 10^2$	$1 \cdot 10^2$	$2 \cdot 10^7$	$1 \cdot 10^9$	7
Li-Pb	500	$1.5 \cdot 10^{-2}$	$2.1 \cdot 10^1$	$1.5 \cdot 10^3$	$7 \cdot 10^2$	$9 \cdot 10^2$	$1 \cdot 10^7$	$4 \cdot 10^8$	1
Li-Sb	450	$2.4 \cdot 10^{-2}$	$6.9 \cdot 10^1$	$2.8 \cdot 10^3$	$3 \cdot 10^2$	$3 \cdot 10^2$	$1 \cdot 10^7$	$5 \cdot 10^8$	2
Li-Se	375	$1.0 \cdot 10^2$	$6.3 \cdot 10^3$	$6.2 \cdot 10^1$	$9 \cdot 10^2$	$8 \cdot 10^4$	$3 \cdot 10^5$	$2 \cdot 10^7$	0.1
Li-Sn	400	$9.8 \cdot 10^{-3}$	$8.4 \cdot 10^1$	$8.5 \cdot 10^3$	$3 \cdot 10^2$	$2 \cdot 10^2$	$4 \cdot 10^7$	$2 \cdot 10^9$	4
Li-Te	475	$1.7 \cdot 10^{-1}$	$8.4 \cdot 10^1$	$4.8 \cdot 10^2$	$3 \cdot 10^3$	$3 \cdot 10^4$	$2 \cdot 10^7$	$9 \cdot 10^8$	0.4
Li-Zn	486	$2.8 \cdot 10^{-2}$	$6.3 \cdot 10^2$	$2.2 \cdot 10^4$	$2 \cdot 10^2$	$8 \cdot 10^1$	$5 \cdot 10^7$	$5 \cdot 10^9$	10
Mg-Sb	700	$1.7 \cdot 10^{-2}$	$3.0 \cdot 10^1$	$1.8 \cdot 10^3$	$5 \cdot 10^2$	$6 \cdot 10^2$	$3 \cdot 10^6$	$4 \cdot 10^8$	20
Na-Bi	550	$1.0 \cdot 10^{-2}$	$6.1 \cdot 10^1$	$6.0 \cdot 10^3$	$1 \cdot 10^3$	$2 \cdot 10^3$	$5 \cdot 10^7$	$9 \cdot 10^9$	10
Na-Hg	275	$3.7 \cdot 10^{-3}$	6.4	$1.7 \cdot 10^3$	$1 \cdot 10^4$	$2 \cdot 10^4$	$1 \cdot 10^8$	$1 \cdot 10^{10}$	10
Na-Pb	575	$1.2 \cdot 10^{-2}$	$2.8 \cdot 10^1$	$2.4 \cdot 10^3$	$7 \cdot 10^2$	$8 \cdot 10^2$	$1 \cdot 10^7$	$2 \cdot 10^9$	10
Na-Sn	625	$6.2 \cdot 10^{-3}$	$2.1 \cdot 10^1$	$3.4 \cdot 10^3$	$3 \cdot 10^2$	$2 \cdot 10^2$	$1 \cdot 10^7$	$9 \cdot 10^8$	10

assuming an unstable length of half the layer thickness and the temperature difference proposed in Eq. (15):

$$Ra^{(E)} \approx \frac{g\beta_T^{(E)}\rho_{el}^{(E)}j^2(\Delta h^{(E)})^5}{64k^{(E)}\mathcal{D}_T^{(E)}\nu^{(E)}} = Ra_H. \qquad (17)$$

This formulation is free of parameters of the other layers and consistent with previous work on internally heated convection [36]. Kulacki and Goldstein [37] provided a complete description of the stability of internally heated layers subject to different combinations of thermal and mechanical boundary conditions. In our application, the electrolyte is mechanically and thermally coupled with good heat conductors (liquid metal electrodes). The conductivities and thicknesses of the electrodes, as well as any localised cooling or heating play a role for the onset of thermal convection within the molten salt. Due to the low and comparable thermal resistance of the two layers, we assume an idealised condition in which the two interfaces are assumed isothermal at the same temperature. The critical Rayleigh numbers in this condition of rigid-rigid and free-free interfaces are respectively 583 and 266 [37]. In a similar arrangement, Sparrow et al. [35] show that the critical Rayleigh number for rigid interfaces is bounded between 560 and 583 for sufficiently conductive boundaries.

These critical Rayleigh numbers were computed for layers infinitely extended in lateral direction. In contrast, the layers of an LMB are bounded by walls, often assumed to be adiabatic. Confinement effects can play a role, possibly increasing the critical Rayleigh number. Ra_{crit} is a decreasing function of the aspect ratio of the layer $\Gamma^{(i)} = \frac{L}{\Delta h^{(i)}}$, in which L denotes the lateral extension. According with studies in classical Rayleigh-Bénard convection [38, 39], the critical Rayleigh number approaches the infinite layer one with the scaling $(Ra_{crit} - Ra_{crit,\infty}) \propto \Gamma^{-2}$. For small aspect ratio $\Gamma \to 0$, Ra_{crit} increases rapidly as Γ^{-4} [39], but this should not be the case for layers of an LMB. In conclusion, the previously gathered results are representative for layers with a high aspect ratio $\Gamma > 4$. Rather than that, for low aspect ratio layers, $Ra_{crit,\infty}$ provides only a lower bound below which no thermal convection is expected. The aspect ratio plays a similar role for the critical Rayleigh number of internally heated convection [40]. The critical value proposed for the electrolyte layer should be suitably descriptive, due to the high aspect ratio of this layer.

In order to get an impression of the relevance of thermal convection in realistic LMBs, we apply the critical Rayleigh numbers to the Li||Bi cell

studied here. The threshold current density, which corresponds to the critical Rayleigh number can be computed as function of the layer thickness and material properties using for the temperature difference an analytical model of pure conduction (e.g. [17]), or by Eq. (14) and Eq. (15). The results, as illustrated in Figure 2, show clearly that thermal convection in the negative electrode is not guaranteed. It will appear only in thick layers. Using typical moderate current densities in the order of $0.25\,\mathrm{A\,cm^{-2}}$ the electrolyte layer needs to be fairly thick as well for convection to set in, see Figure 2b. An efficient operation of the cell in terms of a low ohmic overpotential ($\eta_\Omega = \rho_{\mathrm{el}}j\Delta h^{(\mathrm{E})}$) [1] requires thin electrolytes, which does not guarantee flow will appear in the latter. The two simple formulae (Eq. (14), Eq. (15)) provide a good approximation compared to the more complex analytical model of pure conduction and can be used for predicting the temperature differences in the cell.
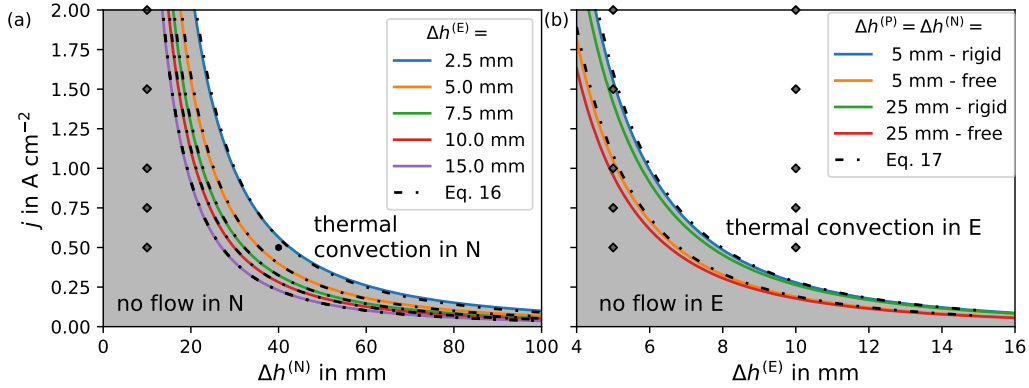

Figure 2: Critical current density and layer heights for the onset of convection in the negative electrode (a) and electrolyte (b). The layers are assumed to be infinitely extended in the lateral directions. If not otherwise specified, the layers are 10 mm thick; for the material properties refer to Tab. 3. Continuous lines are computed with the pure diffusion model of [17]. The dark grey rhombi correspond to the parameters used for the numerical studies `HARC`. The black hexagon in the left figure correspond to the negative electrode of the `LARC` simulation.

3. Numerical model

The equations described in §2.1, §2.2 and §2.3 are discretized using the finite volume method, in the framework provided by the C++ library Open-FOAM [41, 42]. The parent-child mesh strategy is applied to model the

three-layer system with flat interfaces [43, 44]. This means that in addition to the global mesh for the full domain, child meshes for each layer are generated. Material properties are treated as field values and are assigned to each mesh point. A technique called "mapping" is used to exchange field data between the different domains and meshes. For every time step, the system of equations is solved consecutively, with the following procedure: (a) The advection-diffusion equation for the temperature, Eq. (3), is first solved on the parent mesh (full domain). Continuity of temperature and heat flux at the interfaces are automatically enforced by this equation. (b) In the second step, the mass transport equation, Eq. (1), is solved only in the positive electrode (child mesh). The interface between the positive electrode and the electrolyte is treated as a boundary for this equation. (c) Following these two steps, the new density for the buoyancy force is computed and mapped to each domain. (d) Finally, the Navier-Stokes equations are solved sequentially in the negative electrode, the electrolyte and the positive electrode. In order to ensure the mechanical coupling at the common interfaces, appropriate velocity interface conditions are required, as described in §3.1. Knowing that the mechanical coupling is performed in an explicit way (as boundary conditions), the Navier-Stokes equations need to be solved several times in each phase until reaching convergence. Numerical simulations were conducted in parallel over distributed processors. To ensure that each processor has a subset of each region and interface, the domain was decomposed in vertical stripes.

3.1. Discretisation of the mechanical layer coupling

In the OpenFOAM framework, the mechanical layer coupling must be ensured by ad hoc interface conditions. The latter we base here on a simplified version of Eq. 29 by Tukovic and Jasak [45], neglecting the effects of a moving mesh and of surface tension. The exact derivation is the following: the interface conditions for the velocity of a fluid 1 and 2 at a coupled interface read

$$\boldsymbol{u}_{\mathrm{f1}} = \boldsymbol{u}_{\mathrm{f2}}, \tag{18}$$

$$\boldsymbol{u} \cdot \boldsymbol{n} = 0, \tag{19}$$

$$\mu_1 \nabla \boldsymbol{u}_{\mathrm{t1}} \cdot \boldsymbol{n}_1 = \mu_2 \nabla \boldsymbol{u}_{\mathrm{t2}} \cdot \boldsymbol{n}_2, \tag{20}$$

with $\boldsymbol{u}_{\mathrm{f}}$ denoting the velocity at the face between fluid 1 and 2, $\boldsymbol{u}_{\mathrm{t}}$ the tangential velocity in the cell centre, $\boldsymbol{u}_{\mathrm{tf}}$ the tangential velocity at the face,

14

$\boldsymbol{n}$ the face normal vector and μ the dynamic viscosity. By combining the last two boundary conditions, we find

$$\mu_1 \frac{\boldsymbol{u}_{\text{t1}} - \boldsymbol{u}_{\text{tf}}}{\delta_1} = \mu_2 \frac{\boldsymbol{u}_{\text{tf}} - \boldsymbol{u}_{\text{t2}}}{\delta_2}, \tag{21}$$

with δ denoting the distance between cell centre and face. This leads to

$$\boldsymbol{u}_{\text{tf}} = w \cdot \boldsymbol{u}_{\text{t1}} + (1 - w) \cdot \boldsymbol{u}_{\text{t2}} \tag{22}$$

with the weighting factor

$$w = \frac{\delta_2 \cdot \mu_1}{\delta_1 \mu_2 + \delta_2 \mu_1}. \tag{23}$$

As a tangential velocity can be defined as

$$\boldsymbol{u}_{\text{t}} = \boldsymbol{u} \cdot (\boldsymbol{I} - \boldsymbol{nn}), \tag{24}$$

the boundary condition for the velocity at the interface might be written as

$$\boldsymbol{u}_{\text{tf}} = w \cdot \boldsymbol{u}_1 \cdot (\boldsymbol{I} - \boldsymbol{nn}) + (1 - w) \cdot \boldsymbol{u}_2 \cdot (\boldsymbol{I} - \boldsymbol{nn}) = (\boldsymbol{I} - \boldsymbol{nn}) \cdot (w \cdot \boldsymbol{u}_1 + (1 - w) \cdot \boldsymbol{u}_2), \tag{25}$$

in which $\boldsymbol{I}$ denotes the identity matrix. The layer coupling increases the computational cost by a factor between 2 and 5 with respect to a decoupled simulation.

4. Material properties and geometry

We focus in the following on the well-investigated Li||Bi LMB at the reference temperature T_{ref} of $450\,^\circ$C in order to facilitate comparison of our results with previous literature [17]. Considering the excellent availability of material properties, we use an eutectic LiCl-KCl electrolyte, although KCl is known to be unstable in contact with Li at higher temperature [46]. Tab. 3 gives an overview of the material properties of the three liquids. Most of the properties of the Li-Bi alloy are not exactly known. Therefore, the alloy density and the solutal expansion coefficient have been estimated using Vegard's law as suggested by Fazio et al. [32]. We assume a reference molar fraction of $x_{\text{Li}} = 20\,\%$, which corresponds to a Li-mass concentration of $70.62\,\text{kg}\,\text{m}^{-3}$. While the specific heat capacity is mass-weighted between Li and Bi according to the Neummann-Kopp law [33], the kinematic viscosity

Table 3: Thermodynamic and transport properties for a Li‖Bi LMB at $T_{\mathrm{ref}} = 450\,°\mathrm{C}$. The alloy properties have been calculated for a Li-molar fraction of $20\,\%$. c_p is the specific heat capacity, which is used to compute the thermal diffusivity as $\mathcal{D}_{\mathrm{T}} = k(\rho_{\mathrm{ref}}c_p)^{-1}$.

quantity	unit	N - Li	E - LiCl-KCl	P - Li-Bi	source
ρ_{ref}	$\mathrm{kg\,m^{-3}}$	$4.911 \cdot 10^2$	$1.648 \cdot 10^3$	$8.576 \cdot 10^3$	[32, 47, 48]
c_p	$\mathrm{J\,kg^{-1}\,K^{-1}}$	$4.237 \cdot 10^3$	$1.330 \cdot 10^3$	$1.7 \cdot 10^2$	[32, 47, 48]
k	$\mathrm{W\,m^{-1}\,K^{-1}}$	$5.218 \cdot 10^1$	$6.904 \cdot 10^{-1}$	$1.421 \cdot 10^1$	[32, 47, 49]
ρ_{el}	$\Omega\,\mathrm{m}$	$3.27 \cdot 10^{-7}$	$6.358 \cdot 10^{-3}$	$1.39 \cdot 10^{-6}$	[32, 47, 48]
$\mathcal{D}_{\mathrm{T}}$	$\mathrm{m^2\,s^{-1}}$	$2.51 \cdot 10^{-5}$	$3.15 \cdot 10^{-7}$	$9.75 \cdot 10^{-6}$	
Pr		$2.84 \cdot 10^{-2}$	6.29	$1.34 \cdot 10^{-2}$	
ν	$\mathrm{m^2\,s^{-1}}$	$7.13 \cdot 10^{-7}$	$1.983 \cdot 10^{-6}$	$1.304 \cdot 10^{-7}$	[32, 47, 48]
β_{T}	$\mathrm{K^{-1}}$	$1.923 \cdot 10^{-4}$	$3.2 \cdot 10^{-4}$	$1.362 \cdot 10^{-4}$	[32, 47, 50]
$\beta_{\rho_{\mathrm{A}}}$	$\mathrm{m^3\,kg^{-1}}$			$2.122 \cdot 10^{-3}$	[32, 47]
$\mathcal{D}_{\mathrm{AB}}$	$\mathrm{m^2\,s^{-1}}$			$7 \cdot 10^{-9}$	[3]
$\mathcal{M}_{\mathrm{A}}$	$\mathrm{kg\,mol^{-1}}$	$6.94 \cdot 10^{-3}$			[51]
Sc				18.6	

is molar weighted [17]. Thermal and electrical conductivity of the alloy are assumed to be equal to the one of pure Bi at the reference temperature.

In order to resolve the flimsy plumes of solutal convection sufficiently – and taking into account the performance limitations of the finite volume solver – we confine our study to two-dimensional simulations in Cartesian coordinates. The geometry resembles the one shown in Figure 3. The thickness of the electrolyte is bounded by safety and efficiency reasons (see [17] details); here we use 5 and 10 mm. The necessary negative and positive electrode layer heights are determined by the desired composition of the positive electrode in the discharged state. Assuming that all Bi of the positive electrode can be converted into the intermetallic phase Li$_3$Bi, a negative electrode height of about 20 mm would be sufficient. A more common approach is to discharge only in the liquid phase region of the Li-Bi phase diagram ($x_{\mathrm{Li}} \lesssim 40\,\%$ at $450\,°\mathrm{C}$). This would result in a minimum negative electrode height of approximately 4 mm required to fully discharge a cell containing a 10 mm thick positive electrode. Here, we investigate two configurations both with a 10 mm positive electrode, referred to as `LARC` (low aspect ratio cell) and `HARC` (high aspect ratio cell), respectively. The `LARC` has a 40 mm thick

negative electrode, see Figure 3. In this configuration, thermal convection is also expected in the negative electrode at a current density of $0.5\,\mathrm{A\,cm^{-2}}$ (see the black hexagon in Figure 2a). The high aspect ratio cell with 10 mm thick negative electrode is used to study the effect of solutal convection on internally heated convection. Geometrical dimensions and applied current densities of the different configurations studied are collected in Tab. 4.
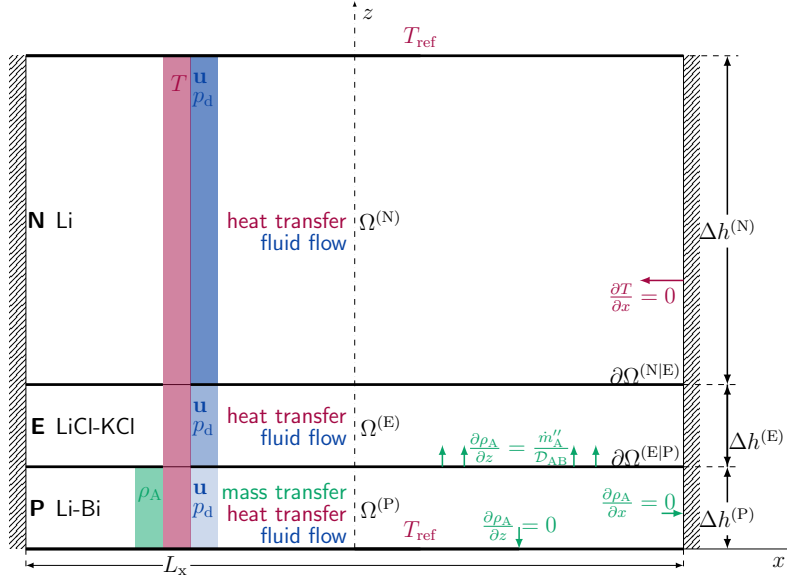

Figure 3: Sketch of the 2D liquid metal battery model with temperature and concentration boundary conditions. The temperature is solved on the parent mesh (full domain), and the other equations on the child meshes (single regions).

Table 4: Simulations list, geometry and current density. HT: heat transfer, MT: mass transfer.

name	L_x	$\Delta h^{(P)}$	$\Delta h^{(E)}$	$\Delta h^{(N)}$	j	properties
	mm	mm	mm	mm	$\mathrm{A\,cm^{-2}}$	
HT_PS	135	45	10	45	0.5	[16]
MT_SEM	40	10	10	10	0.5	Tab. 3
LARC	80	10	10	40	0.5, -0.5	Tab. 3
HARC_H10	80	10	5	10	0.5, 0.75, 1.0, 1.5, 2.0	Tab. 3
HARC_H5	80	10	10	10	0.5, 0.75, 1.0, 1.5, 2.0	Tab. 3

5. Comparison with spectral solvers

In the absence of a suitable comparative case for the full problem, validation of our model is performed separately for thermal and solutal convection, each by comparing the OpenFOAM simulations with results of a pseudo-spectral and a Fourier-spectral-element code respectively.

5.1. Thermal convection

The simulation of thermal convection in a three-layer LMB done with a pseudo-spectral code by Köllner et al. is employed here as a reference. This test case has already been used by Personnettaz et al. [17]. The solver relies on a spatial discretization in Fourier modes on the horizontal plane and Chebychev polynomials in the vertical direction [16, 52]. The horizontal discretization requires periodic boundary conditions at the lateral walls. We enforce the same boundary conditions also in our OpenFOAM simulation to allow for comparison.

The same cell and material properties as the ones studied by Köllner et al. [16] are used here: a Li||Pb-Bi LMB operating at $500\,°C$. The geometry and current density are collected in Tab. 4, with the simulation being denoted as `HT_PS`. The velocity and temperature distributions, illustrated in Figure 4a-b, show a clear resemblance between both numerical codes. By averaging the velocity spatially along the x-coordinate, and thereafter over a time of $50\,s$, we obtain the vertical velocity profile shown in Figure 4c. Very similar as in a recent publication [17], we find that a mesh resolution of 300 control volumes over the lateral size yields a converged velocity profile. Taking the average velocity in steady state condition (over space, and $50\,s$ again) we basically obtain the same result – see Figure 4d.

5.2. Solutal convection

As a test case for solutal convection, we model the positive electrode of a Li||Bi LMB, as illustrated in Figure 5. The dimensions are given in Tab. 4 (test case `MT_SEM`); the applied current density is $0.5\,A\,cm^{-2}$. The comparison is performed against a 2D simulation in Cartesian coordinates done with the Fourier-spectral element code Semtex [53]. In this framework, a grid independent solution was reached using 32 elements in vertical direction with 12x12 polynomials per element. In order to perform the comparison, the boundary condition at the positive electrode/electrolyte interface is set to no-slip in both solvers. The required grid resolution for solutal convection is
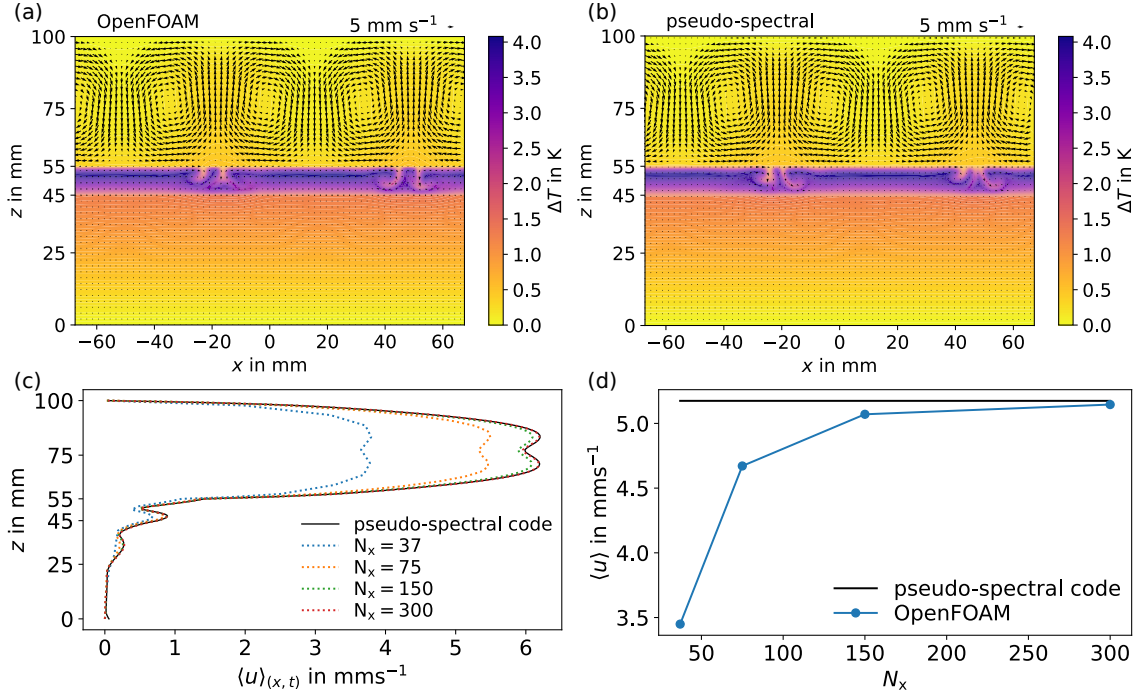
Figure 4: Validation of thermal convection: (a) velocity and temperature distribution of OpenFOAM, (b) the same for the pseudo-spectral code at t = 998 s. (c) Volume averaged velocity and (d) space and time-averaged vertical velocity profile as a function of the lateral mesh resolution. Simulation HT_PS.

substantially higher than for thermal convection due to the lower diffusivity. Especially the plume number and width depend crucially on the mesh resolution, as can be observed in Figure 5a-d. Fortunately, integral quantities, as the average mass concentration at the electrolyte interface, are much less sensitive to the grid resolution. This means, even if the plumes structure is not perfectly resolved, the positive electrode is well mixed in any way. Therefore, the Li interface-concentration results are fairly similar even for coarser meshes – as illustrated in Figure 5e-f.

Considering that within each time step the equation system needs to be solved several times due to the explicit interface coupling, it is extremely challenging to obtain the high accuracy of the spectral codes with Open-FOAM in reasonable computational time. Furthermore, solutal convection in the regime studied shows a strong dependence on initial condition and level of numerical noise. In conclusion, we select a mesh able to capture the
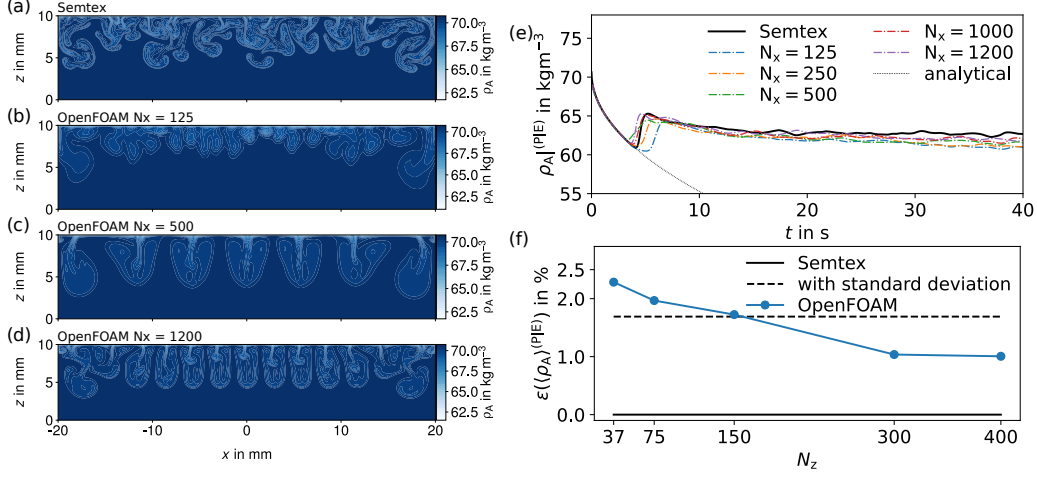
19

Figure 5: Comparison of solutal convection: (a) concentration distribution obtained with Semtex and (b-d) OpenFOAM at different grid resolutions at $t = 6.5\,$s, (e) time evolution of the mean mass concentration of Li at the interface $\partial\Omega^{(P|E)}$ and (f) error of the Li interface concentration compared to Semtex, if averaged over the last $15\,$s.

main flow structures as well as integral quantities. The cell is meshed with at least 600 control volumes in the horizontal direction and 200 along the positive electrode's vertical extension. The mesh in normal direction to the cell walls and to the interfaces as well as in the positive electrode is strongly refined.

6. Results & discussion

We first present results of pure solutal convection in the three-layer system. Then, we move to the interaction of heat and mass transfer.

6.1. Solutal convection

We first present results for purely solutal convection in the `LARC` cell – for the dimensions, see Tab. 4. As reported before, the formation of the initial plumes involves three distinct phases: first, we observe a quasi-stable state, where a concentration boundary layer builds up. This layer is well described by the pure diffusion solution, see Figure 6. Shortly after, the boundary layer becomes unstable, and finally small plumes break rapidly out of the layer as shown in Figure 6b [54]. The whole process takes only 4s. As often observed before, the spatial wavelength increases then with time due to merging of

20

several plumes into larger convection cells [55, 56] – this happens in our case within 3 seconds (Figure 6e). After less than $10\,\mathrm{s}$, the complete positive electrode is already well mixed. The secondary vortices, which develop due to viscous coupling in the electrolyte and in the negative electrode layer turn as expected in opposite direction (Figure 6a) [57]. The mean averaged flow velocity in the positive electrode reaches $5\,\mathrm{mm\,s^{-1}}$, in the electrolyte $1\,\mathrm{mm\,s^{-1}}$ and in the negative electrode only $0.1\,\mathrm{mm\,s^{-1}}$ (Figure 6c). Figures 6f-h illustrate the vertical component of the velocity over time along a horizontal line in the middle of each layer. Obviously, the number of convection cells is very similar within the three phases. Flow starts first in the positive electrode, slightly later in the electrolyte and finally in the negative electrode. Momentum is effectively transferred across the layers.

The most important conclusions of our example are that solutal convection needs only a few seconds to drive strong flow in the positive electrode and that it mixes the electrolyte layer efficiently. There, the velocities reach 20% of the mean averaged velocity of the positive electrode.

6.2. Thermal convection and mass transport

The effect of thermal convection on mixing and cell efficiency has been discussed controversially in the past. Kelley & Sadoway [13] as well as Beltrán [14] suggested that bottom heating might lead to mm-scale velocities in the positive electrode. Shen & Zikanov [15] found that even the flow in the electrolyte might induce velocities in the order of $0.3\,\mathrm{mm\,s^{-1}}$ in the positive electrode by viscous coupling in small LMBs; they further predicted that convection will be much faster in large cells. Moreover, it has been shown that electrochemical heating might even lead to an unstable temperature profile in the positive electrode [17] and that anti-convection might appear, as well [16]. However, all these studies neglected the interaction with mass transport that is always present in the positive electrode during operation.

We focus our first investigations on the `LARC` setup, with the dimensions given in Tab. 4, starting with discharge and then studying charge. As already discussed, during discharge, a stable density stratification forms in the positive electrode due to the concentration, and to smaller extent due to the temperature distribution. We study this phase using a current density of $-0.5\,\mathrm{A\,cm^{-2}}$. The coupling with the electrolyte is the only source of motion in the positive electrode. As the latter is too weak, the flow is strongly damped by the presence of the stable stratification. In Figure 7a we observe that the velocity in the positive electrode at discharge (red dots) is more than
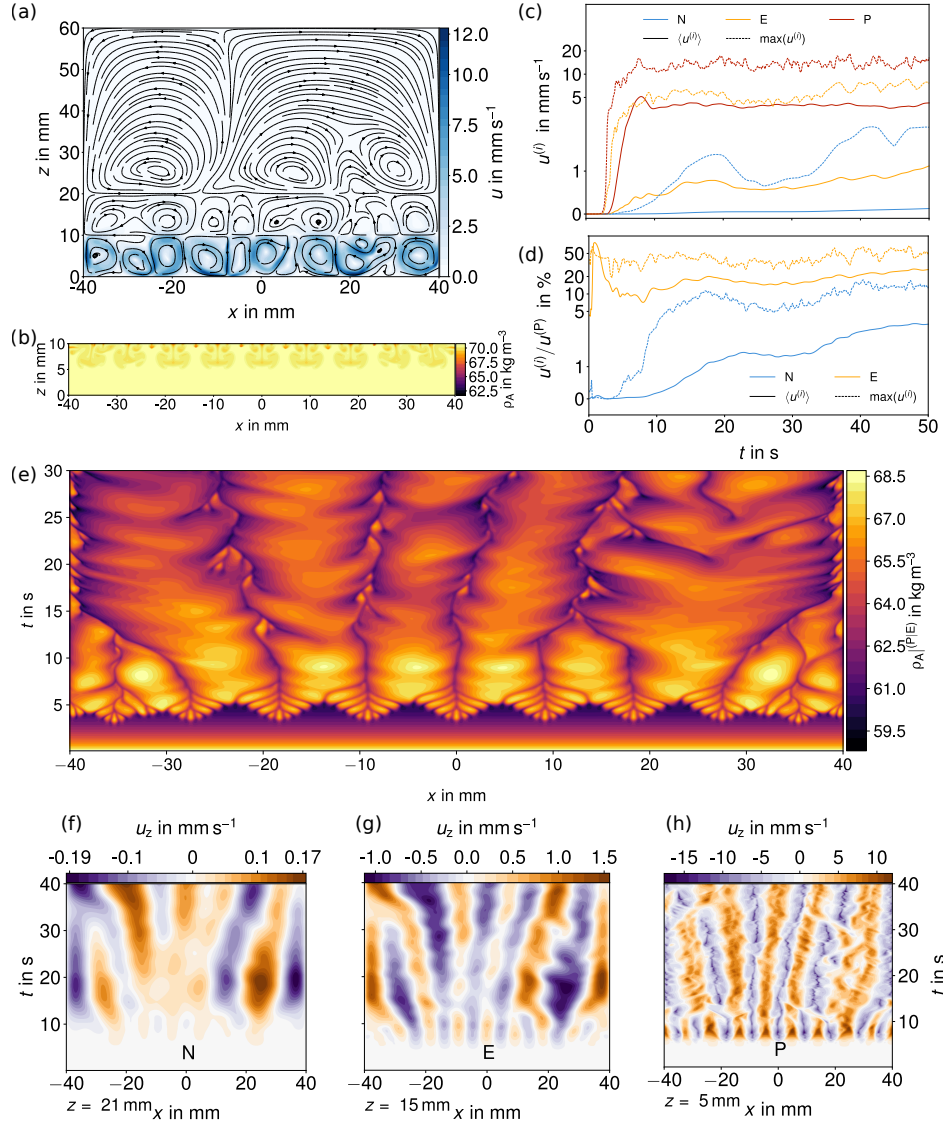
Figure 6: Flow structure and magnitude at 30 s (a), mass concentration distribution at 5.5 s (b), maximum and volume averaged velocity (c), relative velocity compared to the one in the positive electrode (d), mass concentration at the positive electrode/electrolyte interface (e) and vertical velocity over a horizontal line in the negative electrode (f), electrolyte (g) and positive electrode (h). Simulation `LARC`.

one order of magnitude less than in the case of pure thermal convection (red line). The concentration distribution in the positive electrode is unperturbed

and follows exactly the one predicted by the analytical diffusion solution, see Figure 7b [17]. The mean velocities in the other layers are not substantially affected, as shown in Figure 7a. Finally, also the temperature distribution in the cell is similar to the one in the presence of pure thermal convection, Figure 7c-d, as well.
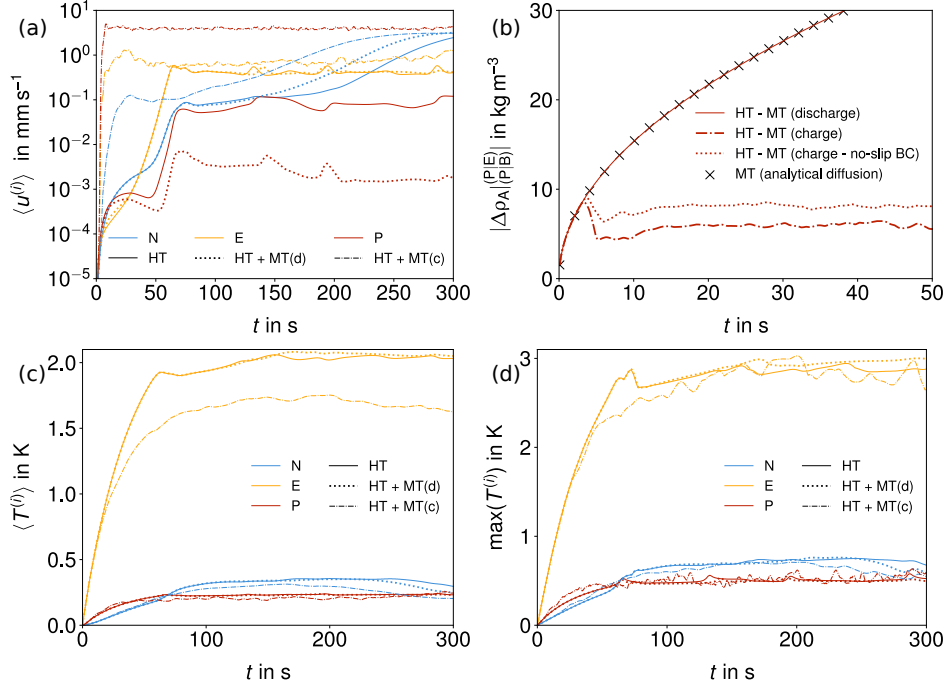
Figure 7: Volume averaged velocity (a), volume averaged temperature (c) and maximum temperature (d) in the three layers in presence of pure thermal convection (HT), during discharge (HT + MT (d)) during charge (HT + MT (c)). Average concentration difference between bottom wall (P|B) and positive electrode/electrolyte interface (P|E) (b) during discharge, charge and charge with a rigid interface. `LARC` setup.

When switching to charge, solutal flow occurs after only few seconds and establishes vigorous motion in the positive electrode as shown in Figure 7a. In previous investigations, the electrolyte/positive electrode interface had been replaced by a no-slip boundary condition, when modelling the positive electrode alone [3, 12]. Our more realistic multi-layer model shows that the concentration difference within the positive electrode is now smaller compared to the single region simulation, see Figure 7b. Obviously, replacing the electrolyte/positive electrode interface by a no-slip boundary condition

attenuates flow and mixing too much, and overestimates therefore the mass transport overpotential.

Solutal convection in the positive electrode is immediately mixing the electrolyte layer. Flow there appears ten times earlier than in the scenario with pure thermal convection. The mean temperature in the electrolyte is reduced by the presence of solutal convection, as shown in Figure 7c.

Overall, solutal convection plays two roles: firstly it is efficiently transporting and dissipating heat through the positive electrode, acting as a forced convection source at the positive electrode/electrolyte interface. And, second, it is mixing the electrolyte by means of the mechanical coupling. In the LARC setup, the height of the negative electrode of 40 mm leads to a thermal Rayleigh number that exceeds the critical value for onset of Rayleigh-Bénard convection even for the relatively low Joule heat produced by a current density of $0.5\,\mathrm{A\,cm^{-2}}$ (Figure 2, left). The electrolyte layer then essentially acts as a heater at the lower interface of the negative electrode. Goluskin (case RB3, [58]) studied a similar configuration. The typical regular convection rolls of low-Ra Rayleigh-Bénard convection develop, as shown in Figure 8b. The growth phase needs considerable time, because first a sufficient temperature gradient has to be established. However, solutal convection is able to introduce disturbances in the top layer, which can trigger an earlier onset. Similar convective rolls were observed in numerical simulation of cuboid Li||Bi cell by Personnettaz et al. [17]. These large scale structures are influenced by the shape of the container (cuboid or cylinder). Our 2D Cartesian simulations may therefore not accurately reflect the real flow structures.

Viscous coupling at the interfaces is important for the LARC geometry as well. Especially for the fully developed flow, the negative electrode takes then the driving role and influences the flow in the electrolyte to a large extent. This "dragging mode" [59] contributes to the formation of relatively broad vortex cells in the electrolyte.

Computing the temporal mean value of the volume-averaged kinetic energy as [15]

$$\frac{E_{\mathrm{kin}}}{\rho} = \frac{1}{V} \int_V |\boldsymbol{u}|^2 dV \tag{26}$$

we find that the lowest energy can be observed in the electrolyte for the LARC case, see Figure 8. Since Joule heating is proportional to the square of the current density, but mass transfer depends only linearly on j, we expect that the maximum velocities in the negative electrode exceed those in the positive
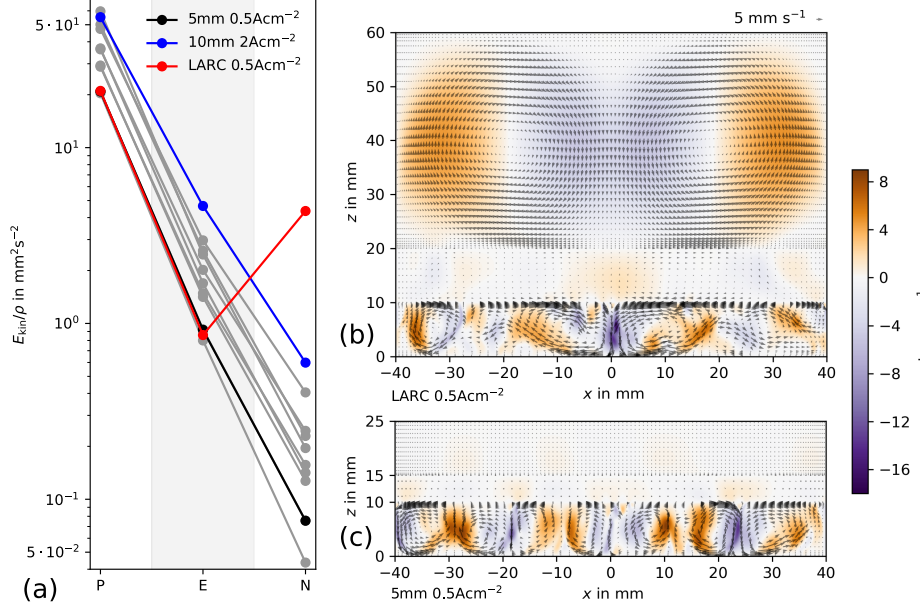
24

Figure 8: Kinetic energy in the three layers of the cell for different current densities and aspect ratios (a). Snapshots of two flow fields for the cell with the low aspect ratio negative electrode (LARC, b) and for a HARC cell (c) under charge with $0.5\,\mathrm{A\,cm^{-2}}$.

electrode for the LARC geometry if the current density exceeds $0.5\,\mathrm{A/cm^2}$.

6.3. Interaction of thermal and solutal convection in high aspect ratio cells

We limit the discussion in this section to the charging phase in vertically symmetric cells. The geometry is denoted as "high aspect ratio cell" (HARC) in the text. Tab. 4 provides the dimensions and current density, which are also illustrated by grey rhombi in the right diagram of Figure 2. The setup used here is much closer to real cells, as already discussed in §4. Looking at Figure 8a it can be seen that the temporal mean value of the volume-averaged kinetic energy decreases monotonically from the positive electrode over the electrolyte to the negative electrode.

Within all simulations, the solutal convection's kinetic energy in the positive electrode exceeds that in the other layers by at least an order of magnitude.

In all cases, the layer coupling is dominated by viscous forces as already found by other authors [15, 16] for thermal convection in liquid metal batteries. The horizontal velocity components near the interfaces go into the
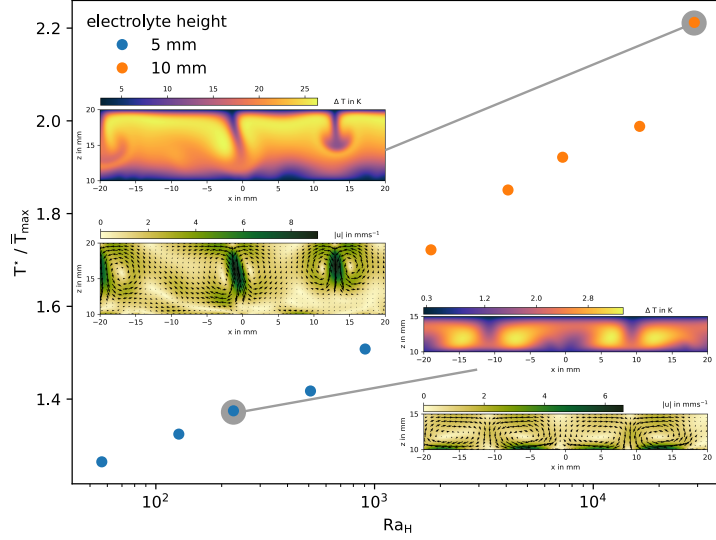
Figure 9: Convective cooling parameter $T^\star/\overline{T}_{\max}$ as a function of Ra_{H} for two different electrolyte heights. The two insets show snapshots of the temperature and velocity distribution of the fully developed flow in the electrolyte at the two parameter sets encircled in grey. In horizontal direction only the central part of the electrolyte is shown. `HARC` setup.

same direction on both sides of the interface, and interface normal velocity components mirror each other.

The total heat released in the electrolyte grows with the electrolyte thickness and the current density. While the negative electrode's Rayleigh number is smaller than the critical value for all current densities considered, the electrolyte's Rayleigh number exceeds the critical value for rigid-rigid boundaries only for $j = 2\,\mathrm{Acm}^{-2}$ and a 5 mm thick electrolyte and for all current densities, if the electrolyte thickness amounts to 10 mm.

Thermally driven convection in LMBs means classical Rayleigh-Bénard convection in the negative electrode, but internally heated convection in the electrolyte. The former is well investigated, meticulously described in almost all details and still subject of intense research; the latter received much less attention but is nevertheless important for topics as diverse as mantle convection, nuclear reactor engineering, and astrophysics. For a relatively recent comprehensive review of both, see [58].

Solutal convection provides a momentum source to the electrolyte via viscous coupling at the positive electrode/electrolyte interface. The influence of this momentum source on the flow in the electrolyte is visible in the flow

26

structure and the integral properties of the thermal convection as can be seen in Figure 9. It shows the convective cooling parameter $T^\star/\overline{T}_{\max}$ as defined by Peckover and Hutchinson [60] vs. the Rayleigh number based on the Joule heat release and the electrolyte layer's half height [36] described by Eq. (17). The convective cooling parameter is the ratio of the maximum temperature $T^\star$ that would occur if heat transport were purely conductive, to the maximum value of the (height dependent) temperature profile $\overline{T}_{\max}$ in the fully developed flow averaged over time and in horizontal direction. The location of $T^\star$ and $\overline{T}_{\max}$ is marked in the temperature profiles of Figure 10. Even for the smallest Ra_{H} ($Ra_{\mathrm{H}} = 56$), the cooling parameter ($T^\star/\overline{T}_{\max} = 1.26$) exceeds one. This signals that convection is present in the electrolyte intensifying heat transfer. The lower inset in Figure 9 ($Ra_{\mathrm{H}} = 226, T^\star/\overline{T}_{\max} = 1.37$) displays snapshots of the instantaneous flow and temperature fields in the midsection ($-20\,\mathrm{mm} < x < 20\,\mathrm{mm}$) of the electrolyte. Despite the Rayleigh number being considerably lower than its critical value, four convection cells are visible in the flow field. They are driven by viscous coupling at the positive electrode/electrolyte interface ($z = 10\,\mathrm{mm}$) where the highest velocities can be observed. The temperature field is modulated by the influence of convection and displays cooler regions where the flow transports cold fluid from the boundaries into the bulk. Thus, the four convection cells leave their footprints in the temperature field and alter it considerably with respect to the purely conductive case. While the velocities in the upper part of the electrolyte are smaller than that in the lower part, the cells as well as their thermal footprint occupy the entire electrolyte region.

The upper inset in Figure 9 ($Ra_{\mathrm{H}} = 28979, T^\star/\overline{T}_{\max} = 2.2$) shows flow and temperature fields of well developed internally heated convection. The flow field looks now quite different and so does the temperature field. While the influence of viscous coupling is still visible at the positive electrode/electrolyte interface, the highest velocities now occur in the plumes descending from the electrolyte/negative electrode interface because of the unstable temperature and thereby density distribution. As characteristic for internally heated convection with heat transfer over both horizontal boundaries, convection is very intense in the upper half of the layer, but damped in the lower one. This is a consequence of the – on average – stable stratification in the lower and the unstable stratification in the upper part of the layer. This asymmetry results in penetrative convection (see, e.g. [61]) where fluid undergoes convective motion in the upper part and penetrates into the lower stably stratified layer. Such a situation leads to irregular motion even for Rayleigh
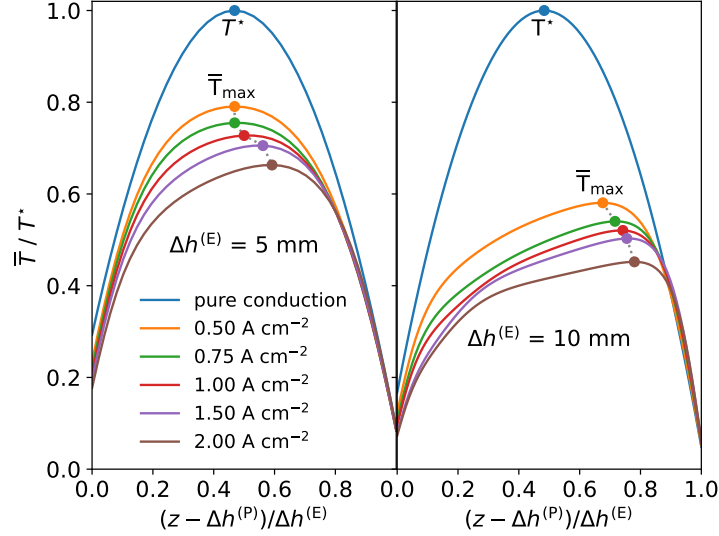
27

Figure 10: Horizontally averaged vertical temperature profiles in the electrolyte normalised with the maximum conductive temperature $T^\star$ for the 5 mm and the 10 mm thick electrolyte and different current densities. `HARC` setup.

numbers close to the critical one as reported by a number of authors, e.g., [62–65] and as observed here as well.

Figure 10 displays the horizontally averaged vertical temperature profiles normalised with the maximum conductive temperature for the two electrolyte heights investigated. As already discussed in connection with Figure 9, we observe convection for the smallest Rayleigh number investigated ($Ra_H = 56$, corresponding to $j = 0.5 \, \text{A cm}^{-2}$ in the 5 mm thick electrolyte). This results in a moderate reduction of the maximum temperatures $\overline{T}_{\text{max}}$ with respect to $T^\star$. However, the shape of the temperature profiles is still relatively symmetric for the 5 mm thick electrolyte with somewhat larger deviations for $j = 1.5 \, \text{A cm}^{-2}$ and $2 \, \text{A cm}^{-2}$. This changes for the 10 mm thick electrolyte with its much higher Rayleigh numbers due to the stronger heat release in the thicker layer. The reduction of $\overline{T}_{\text{max}}$ with respect to $T^\star$ is more pronounced as is the asymmetry of the temperature profiles. The location of $\overline{T}_{\text{max}}$ shifts to almost $(z - \Delta h^{(P)})/\Delta h^{(E)} = 0.8$ for $j = 2.0 \, \text{A cm}^{-2}$. The increase in asymmetry with the heating rate in the electrolyte is again a feature that is to be expected and known from the literature, e.g., [36, 60, 64, 65].

Corresponding to these changes in the mean temperature profiles, the heat transfer conditions at the interfaces change. This is shown in Figure 11.
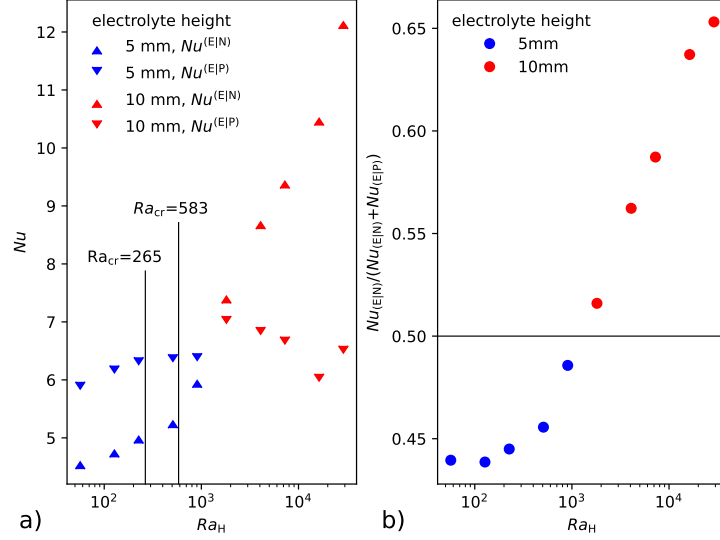
Figure 11: Nusselt numbers for the top and bottom interface of the electrolyte with the electrodes (left) and Nusselt number ratio (right) vs. Rayleigh number for different electrolyte thicknesses. `HARC` setup.

Figure 11a displays the Nusselt numbers at the electrolyte/negative electrode interface ($Nu^{\mathrm{E|N}}$) and at the positive electrode/electrolyte interface ($Nu^{\mathrm{E|P}}$). The Nusselt number definition is that used by Kulacki and Goldstein [36]

$$\mathrm{Nu}^{(\mathrm{E}|i)} = \frac{\Delta h^{(\mathrm{E})} |d\langle T\rangle_{x,t}/dz|^{(\mathrm{E}|i)}}{\overline{T}_{\max} - \langle T\rangle_{x,t}^{(\mathrm{E}|i)}} \text{ for } i = \mathrm{N}, \mathrm{P} \ , \tag{27}$$

with the electrolyte height $\Delta h^{(\mathrm{E})}$, the temperature gradient at the interface $|d\langle T\rangle_{x,t}/dz|^{(\mathrm{E}|i)}$, the maximum temperature in the layer $\overline{T}_{\max}$, and the temperature of the interface $\langle T\rangle_{x,t}^{(\mathrm{E}|i)}$. Internally heated convection with equal temperatures at the horizontal boundaries features typically higher Nusselt numbers on the top of the layer and lower ones on the bottom, see, e.g. [36]. This is in contrast to what we observe for the 5 mm thick electrolyte layer. Here, $Nu^{\mathrm{E|P}}$ exceeds $Nu^{\mathrm{E|N}}$ for all investigated Rayleigh numbers. Since viscous coupling at the lower interface is the only source of convective motion for $Ra_{\mathrm{H}} < \mathrm{Ra_{H, \, crit}}$, stronger convective heat transfer at the lower interface is an expected result for these cases. But even for the higher Ra in the 5 mm thick electrolyte convective heat transport due to viscous coupling outweighs that due to thermal convection.

29

The conditions are reversed for the 10 mm thick electrolyte. As in purely internally heated convection, $Nu^{E|N}$ is larger than $Nu^{E|P}$ for all Ra_H investigated. Thermal convection clearly dominates momentum transfer by viscous coupling. This transition can be observed as well by looking at the flux ratio $Nu^{E|N}/(Nu^{E|N}+Nu^{E|P})$ in Figure 11b. The flux ratio would be 0.5 for the conductive case but lies below this value for the 5 mm thick electrolyte, i.e., more heat is transferred through the positive electrode/electrolyte interface than through the electrolyte/negative electrode interface. For the 10 mm thick electrolyte, the flux ratio is larger than 0.5 because more heat leaves the electrolyte through the top interface than through the bottom one.

7. Summary

As liquid metal batteries (LMBs) operate as concentration cells, mixing is extremely important. After discussing that concentration overpotentials might appear in the positive electrode, we briefly gave an overview on the various flow phenomena being present in LMBs. We showed that different mass transport effects on the cell voltage have already been observed 60 years ago. However, the source of these effects was explained only very recently by Personnettaz et al. [3].

With this background and motivation, we studied the interaction of solutal and thermal convection in a Li||Bi LMB. A brief theoretical analysis suggests that solutal convection will always be able to mix the stable thermal stratification. On the other hand, the thermal flow is not expected to be strong enough to mix the compositionally stably stratified positive electrode. Using critical Rayleigh numbers for an infinitely extended layer from literature, we predicted further that thermal convection will appear only in very thick electrolyte layers and seldomly in the negative electrode.

In order to study the interplay of solutal and thermal convection in more detail, we developed a numerical model with fixed interfaces, solving for the temperature and flow field within the complete cell, and the concentration distribution in the positive electrode. The validation, which was performed by comparison with two (pseudo-)spectral codes, suggests that the mesh resolution for solutal convection needs to be considerably finer than for thermal flow.

In a first step, we simulated solutal convection, which is present only in the positive electrode during the charge phase. We found that it almost instantly produces a very strong mixing effect in the cell. The velocities,

which are induced in the electrolyte via viscous coupling, reach still 20% of the average velocity compared to the positive electrode. Therefore, we deduced that compositional flow mixes both the positive electrode and electrolyte. We further found that it is important to model the mechanically coupled electrolyte/positive electrode interface. Replacing the interface with a simplified no-slip boundary condition attenuates flow and mixing and will therefore overestimate the mass transport overvoltage [3, 10].

In a second step, we simulated thermal convection in discharge. As it appears first in the electrolyte, it is able to mix this region well. However, the viscous coupling is not strong enough to induce any relevant flow in the positive electrode.

Finally, we studied thermal and solutal convection together. We showed that thermal convection needs roughly ten times longer to develop, compared to the solutal flow. The layer coupling is always viscous. While thermal convection does not develop in thin electrolyte layers, except for the highest investigated current density, thick electrolyte layers are always dominated by thermally driven flow. Accordingly, thin electrolyte layers feature relatively regular convection cells during charge. These extend over the full height and are driven by viscous coupling from the positive electrode that is well mixed by solutal convection. In contrast, the Rayleigh numbers of thick electrolyte layers are well above the critical ones for all cases considered. Averaged temperature profiles show a pronounced asymmetry typical for penetrative convection. Nusselt numbers at the upper boundary of the electrolyte layer exceed that at the lower boundary for thick electrolytes. The opposite holds true for thin electrolytes, where viscous coupling drives the most intense flow of the lower boundary and the cooling parameter is smaller than 0.5.

In summary, we would like to stress that solutal convection is a very powerful effect. Although it appears only in the positive electrode at charge, it is able to mix then the electrolyte via viscous coupling at the interface. In contrast, thermal convection can appear only in comparably thick electrolyte layers, but will then allow mixing them during charge and discharge.

Our simulations are limited to 2D Cartesian geometries due to the computational cost of our numerical approach. Extending our work to three dimensional cells will provide relevant insights on the coupling across the layers and the intriguing interplay between heat and mass transport. Furthermore, future models should include thermal and solutal Marangoni effects at the interfaces in order to evaluate their contributions to the mixing of the electrolyte and the electrodes.

31

Acknowledgements

References

[1] H. Kim, D. A. Boysen, T. Ouchi, D. R. Sadoway, Calcium - bismuth electrodes for large - scale energy storage (liquid metal batteries), J. Power Sources 241 (2013) 239–248. `doi:10.1016/j.jpowsour.2013.04.052`.

[2] D. H. Kelley, T. Weier, Fluid mechanics of liquid metal batteries, Appl. Mech. Rev. 70 (2) (2018) 020801. `doi:10.1115/1.4038699`.

[3] P. Personnettaz, S. Landgraf, M. Nimtz, N. Weber, T. Weier, Mass transport induced asymmetry in charge/discharge behavior of liquid metal batteries, Electrochem. Commun. 105 (2019) 106496. `doi:10.1016/j.elecom.2019.106496`.

[4] B. Agruss, H. R. Karas, V. L. Decker, Design and development of a liquid metal fuel cell, Tech. Rep. ASD-TDR-62-1045, General Motors Corporation (1962).

[5] E. J. Cairns, C. E. Crouthamel, A. K. Fischer, M. S. Foster, J. C. Hesson, C. E. Johnson, H. Shimotake, A. D. Tevebaugh, Galvanic Cells with Fused-Salt Electrolytes, ANL-7316, Argonne National Laboratory, 1967.

[6] R. C. Vogel, M. Levenson, E. R. Proud, J. Royal, Chemical engineering division research highlights, Tech. Rep. ANL-7350, Argonne National Laboratory (1967).

[7] M. S. Foster, Laboratory Studies of Intermetallic Cells, in: C. E. Crouthamel, H. L. Recht (Eds.), Regenerative EMF Cells, American Chemical Society, 1967, pp. 136–148.

[8] R. Ashour, D. H. Kelley, A. Salas, M. Starace, N. Weber, T. Weier, Competing forces in liquid metal electrodes and batteries, J. Power Sources 378 (2018) 301–310. `doi:10.1016/j.jpowsour.2017.12.042`.

[9] N. Weber, M. Nimtz, P. Personnettaz, A. Salas, T. Weier, Electromagnetically driven convection suitable for mass transfer enhancement in liquid metal batteries, Appl. Therm. Eng. 143 (2018) 293–301. `doi: 10.1016/j.applthermaleng.2018.07.067`.

[10] W. Herreman, S. Bénard, C. Nore, P. Personnettaz, L. Cappanera, J.-L. Guermond, Solutal buoyancy and electrovortex flow in liquid metal batteries, Phys. Rev. Fluids 5 (7) (2020) 074501. `doi:10.1103/ PhysRevFluids.5.074501`.

[11] N. Weber, M. Nimtz, P. Personnettaz, T. Weier, D. Sadoway, Numerical simulation of mass transfer enhancement in liquid metal batteries by means of electro-vortex flow, J. Power Sources Adv. 1 (2020) 100004. `doi:10.1016/j.powera.2020.100004`.

[12] W. Herreman, C. Nore, L. Cappanera, J.-L. Guermond, Efficient mixing by swirling electrovortex flows in liquid metal batteries, J. Fluid Mech. 915 (2021) A17. `doi:10.1017/jfm.2021.79`.

[13] D. H. Kelley, D. R. Sadoway, Mixing in a liquid metal electrode, Phys. Fluids 26 (5) (2014) 057102. `doi:10.1063/1.4875815`.

[14] A. Beltrán, MHD natural convection flow in a liquid metal electrode, Appl. Therm. Eng. 114 (2016) 1203–1212. `doi:10.1016/j. applthermaleng.2016.09.006`.

[15] Y. Shen, O. Zikanov, Thermal convection in a liquid metal battery, Theor. Comput. Fluid Dyn. 30 (4) (2016) 275–294. `doi:10.1007/ s00162-015-0378-1`.

[16] T. Köllner, T. Boeck, J. Schumacher, Thermal Rayleigh-Marangoni convection in a three-layer liquid-metal-battery model, Phys. Rev. E 95 (2017) 053114. `doi:10.1103/PhysRevE.95.053114`.

[17] P. Personnettaz, P. Beckstein, S. Landgraf, T. Köllner, M. Nimtz, N. Weber, T. Weier, Thermally driven convection in Li||Bi liquid metal batteries, J. Power Sources 401 (2018) 362–374. `doi:10.1016/j.jpowsour.2018.08.069`.

[18] F. Stefani, V. Galindo, C. Kasprzyk, S. Landgraf, M. Seilmayer, M. Starace, N. Weber, T. Weier, Magnetohydrodynamic effects in liquid metal batteries, IOP Conf. Ser. Mater. Sci. Eng. 143 (2016) 012024. `doi:10.1088/1757-899X/143/1/012024`.

[19] H. Kim, D. A. Boysen, J. M. Newhouse, B. L. Spatocco, B. Chung, P. J. Burke, D. J. Bradwell, K. Jiang, A. A. Tomaszowska, K. Wang, W. Wei, L. A. Ortiz, S. A. Barriga, S. M. Poizeau, D. R. Sadoway, Liquid Metal Batteries: Past, Present, and Future, Chem. Rev. 113 (3) (2013) 2075–2099. `doi:10.1021/cr300205k`.

[20] S. Lawroski, R. C. Vogel, V. H. Munnecke, Chemical engineering division summary report, Tech. Rep. ANL-6543, Argonne National Laboratory (1962).

[21] C. E. Crouthamel, H. L. Recht (Eds.), Regenerative EMF Cells, Vol. 64, American Chemical Society, 1967.

[22] H. Shimotake, E. J. Cairns, Bimetallic galvanic cells with fused-salt electrolytes, in: Advances in Energy Conversion Engineering, ASME, Florida, 1967, pp. 951–962.

[23] D. J. Bradwell, Liquid Metal Batteries: Ambipolar Electrolysis and Alkaline Earth Electroalloying Cells, Ph.D. thesis, Massachusetts Institute of Technology (2011).

[24] T. Ouchi, H. Kim, X. Ning, D. R. Sadoway, Calcium-Antimony Alloys as Electrodes for Liquid Metal Batteries, J. Electrochem. Soc. 161 (12) (2014) A1898–A1904. `doi:10.1149/2.0801412jes`.

[25] T. Ouchi, H. Kim, B. L. Spatocco, D. R. Sadoway, Calcium-based multi-element chemistry for grid-scale electrochemical energy storage, Nat. Commun. 7 (2016) 10999. `doi:10.1038/ncomms10999`.

[26] A. Blanchard, Enabling multi-cation electrolyte usage in LMBs for lower cost and operating temperature, Bachelor thesis, Massachusetts Institute of Technology (2013).

[27] B. Agruss, The Thermally Regenerative Liquid-Metal Cell, J. Electrochem. Soc. 110 (11) (1963) 1097–1103.

[28] R. B. Bird, W. E. Stewart, E. N. Lightfoot, Transport Phenomena, Wiley, 2002. `doi:10.1115/1.1424298`.

[29] N. Weber, C. Duczek, G. M. Horstmann, S. Landgraf, M. Nimtz, P. Personnettaz, T. Weier, D. R. Sadoway, Cell voltage model for Li-Bi liquid metal batteries, Appl. Energy, accepted (2021).

[30] L. G. Leal, Advanced Transport Phenomena: Fluid Mechanics and Convective Transport Processes, Cambridge Series in Chemical Engineering, Cambridge University Press, 2007. `doi:10.1017/CBO9780511800245`.

[31] B. B. Alchagirov, F. F. Dyshekova, R. K. Arkhestov, O. K. Kyasova, Surface tension and adsorption of lithium in bismuth-based alloys, Bulletin of the Russian Academy of Sciences: Physics 80 (11) (2016) 1381–1384. `doi:10.3103/s1062873816110071`.

[32] C. Fazio, Handbook on Lead-bismuth Eutectic Alloy and Lead Properties, Materials Compatibility, Thermal-hydraulics and Technologies, Tech. Rep. 7268, Nuclear Energy Agency (2015).

[33] T. Iida, R. I. L. Guthrie, The Thermophysical Properties of Metallic Liquids, Oxford University Press, United Kingdom, 2015.

[34] A. K. Roy, R. P. Chhabra, Prediction of Solute Diffusion Coefficients in Liquid Metals, Metall. Trans. A 19 (1988) 273–279. `doi:10.1007/bf02652536`.

[35] E. M. Sparrow, R. J. Goldstein, V. K. Jonsson, Thermal instability in a horizontal fluid layer: Effect of boundary conditions and non-linear temperature profile, J. Fluid Mech. 18 (4) (1964) 513–528. `doi:10.1017/S0022112064000386`.

[36] F. A. Kulacki, R. J. Goldstein, Thermal convection in a horizontal fluid layer with uniform volumetric energy sources, J. Fluid Mech. 55 (02) (1972) 271–287. `doi:10.1017/s0022112072001855`.

[37] F. A. Kulacki, R. J. Goldstein, Hydrodynamic instability in fluid layers with uniform volumetric energy sources, Appl. Sci. Res. 31 (2) (1975) 81–109. `doi:10.1007/bf01795829`.

[38] E. L. Koschmieder, Bénard cells and Taylor vortices, Cambridge University Press, 1993.

[39] J. Mizushima, Onset of the thermal convection in a finite two-dimensional box, Journal of the Physical Society of Japan 64 (7) (1995) 2420–2432. `doi:10.1143/jpsj.64.2420`.

[40] G. K. Perekattu, C. Balaji, On the onset of natural convection in differentially heated shallow fluid layers with internal heat generation, International Journal of Heat and Mass transfer 52 (19-20) (2009) 4254–4263. `doi:10.1016/j.ijheatmasstransfer.2009.04.006`.

[41] H. Jasak, T. Uroić, Practical Computational Fluid Dynamics with the Finite Volume Method, Springer International Publishing, 2020, pp. 103–161. `doi:10.1007/978-3-030-37518-8_4`.

[42] H. G. Weller, G. Tabor, H. Jasak, C. Fureby, A tensorial approach to computational continuum mechanics using object-oriented techniques, Comput. Phys. 12 (6) (1998) 620–631. `doi:10.1063/1.168744`.

[43] S. B. Beale, H.-W. Choi, J. G. Pharoah, H. K. Roth, H. Jasak, D. H. Jeon, Open-source computational model of a solid oxide fuel cell, Comput. Phys. Commun. 200 (2016) 15–26. `doi:10.1016/j.cpc.2015.10.007`.

[44] N. Weber, P. Beckstein, V. Galindo, M. Starace, T. Weier, Electro-vortex flow simulation using coupled meshes, Comput. Fluids 168 (2018) 101–109. `doi:10.1016/j.compfluid.2018.03.047`.

[45] Ž. Tuković, H. Jasak, A moving mesh finite volume interface tracking method for surface tension dominated interfacial fluid flow, Comput. Fluids 55 (2012) 70–84. `doi:10.1016/j.compfluid.2011.11.003`.

[46] M. S. Foster, S. E. Wood, C. E. Crouthamel, Thermodynamics of Binary Alloys. I. The Lithium-Bismuth System, Inorg. Chem. 3 (10) (1964) 1428–1431. `doi:10.1021/ic50020a019`.

[47] R. W. Ohse (Ed.), Handbook of Thermodynamic and Transport Properties of Alkali Metals, no. 30 in IUPAC Chemical Data Series, Blackwell Scientific, Oxford, 1985.

[48] C. J. Raseman, H. Susskind, G. Farber, W. McNulty, F. Salzano, Engineering experience at Brookhaven National Laboratory in handling fused chloride salts, Tech. Rep. BNL 627, Brookhaven National Laboratory (1960).

[49] G. J. Janz, R. P. T. Tomkins, C. B. Allen, Molten Salts: Volume 4, Part 4 Mixed Halide Melts Electrical Conductance, Density, Viscosity, and Surface Tension Data, J. Phys. Chem. Ref. Data 8 (1) (1979) 125–302. `doi:10.1063/1.555590`.

[50] G. J. Janz, Thermodynamic and transport properties for molton salts: Correlation equations for critically evaluated density, surface tension, electrical conductance, and viscosity data, J. Phys. Chem. Ref. Data 17 (1988).

[51] P. J. Linstrom, W. G. Mallard, NIST Chemistry WebBook, NIST Standard Reference Database Number 69, National Institute of Standards and Technology, Gaithersburg MD, 20899, 2018. `doi:10.18434/T4D30`.

[52] T. Köllner, M. Rossi, F. Broer, T. Boeck, Chemical convection in the methylene-blue–glucose system: Optimal perturbations and three-dimensional simulations, Phys. Rev. E 90 (5) (2014) 053004. `doi:10.1103/PhysRevE.90.053004`.

[53] H. Blackburn, D. Lee, T. Albrecht, J. Singh, Semtex: A spectral element–Fourier solver for the incompressible Navier–Stokes equations in cylindrical or Cartesian coordinates, Comput. Phys. Commun. 245 (2019) 106804. `doi:10.1016/j.cpc.2019.05.015`.

[54] R. J. Goldstein, R. J. Volino, Onset and development of natural convection above a suddenly heated horizontal surface, J. Heat Transf. 117 (4) (1995) 808–821. `doi:10.1115/1.2836296`.

[55] J. Philippi, M. Berhanu, J. Derr, S. Courrech du Pont, Solutal convection induced by dissolution, Phys. Rev. Fluids 4 (10) (2019) 103801. `doi:10.1103/PhysRevFluids.4.103801`.

[56] S. Backhaus, K. Turitsyn, R. E. Ecke, Convective Instability and Mass Transport of Diffusion Layers in a Hele-Shaw Geometry, Phys. Rev. Lett. 106 (10) (2011) 104501. `doi:10.1103/PhysRevLett.106.104501`.

[57] A. Prakash, K. Yasuda, F. Otsubo, K. Kuwahara, T. Doi, Flow coupling mechanisms in two-layer Rayleigh-Benard convection, Experiments in Fluids 23 (3) (1997) 252–261. `doi:10.1007/s003480050108`.

[58] D. Goluskin, Internally Heated Convection and Rayleigh-Bénard Convection, Springer International Publishing, Cham, 2016. `doi:10.1007/978-3-319-23941-5`.

[59] D. Johnson, R. Narayanan, Geometric effects on convective coupling and interfacial structures in bilayer convection, Phys. Rev. E 56 (5) (1997) 5462–5472. `doi:10.1063/1.166384`.

[60] R. S. Peckover, I. H. Hutchinson, Convective rolls driven by internal heat sources, Phys. Fluids 17 (7) (1974) 1369–1371. `doi:10.1063/1.1694897`.

[61] G. Veronis, Penetrative convection, Astrophys. J. 137 (1963) 641–663. `doi:10.1086/147538`.

[62] M. Jahn, H. H. Reineke, Free convection heat transfer with internal heat sources calculations and measurements, in: Proc. International Heat Transfer Conference 5, Tokyo, 1974, pp. 74–78. `doi:10.1615/ihtc5.2950`.

[63] J. C. Ralph, R. McGreevy, R. S. Peckover, Experiments in turbulent thermal convection driven by internal heat sources, in: Heat Transfer and Turbulent Buoyant Convection, Vol. 2, McGraw-Hill, 1976, pp. 587–599.

[64] M. Tveitereid, Thermal convection in a horizontal fluid layer with internal heat sources, Int. J. Heat Mass Transf. 21 (1978) 335–339.

[65] F. A. Kulacki, D. E. Richards, Natural convection in plane layers and cavities with volumetric energy sources, in: S. Kakac, W. Aung, R. Viskanta (Eds.), Natural Convection: Fundamentals and Applications, Hemisphere, Washington, 1985, pp. 179–255.